João P. D. Miranda, Duarte M. N. Rodrigues, Luis A. M. Barros, J. G. Pinto, "DC-DC Power Converter for High Power Solar Photovoltaic System", International Conference on Sustainable Energy for Smart Cities (SESC), 18 Nov 2022, Online.
https://doi.org/10.1007/978-3-031-33979-0_10

DC-DC Power Converter for High Power Solar Photovoltaic System

João P. D. Miranda [*,1], Duarte M. N. Rodrigues[**,1], Luis A. M. Barros[1,2], J. G. Pinto[1,2]

[1] Department of Industrial Electronics – University of Minho, Guimarães – Portugal
[2] ALGORITMI Centre/LASI – University of Minho, Guimarães – Portugal

*Correspondence: pg47332@alunos.uminho.pt
**Correspondence: pg47158@alunos.uminho.pt

Abstract. Worldwide there is an enormous dependence on fossil fuels to produce electricity. Burning fossil fuels results in CO_2 emission into the atmosphere, causing a negative environmental impact. In order to mitigate these problems, there is a need to integrate renewable energy sources into the power grid, namely solar photovoltaic (PV) energy. Power electronics converter solutions for solar PV module interface are vast and have advantages and disadvantages depending on the purpose. In addition, when the purpose is efficiency, it is important to consider the choice of the most appropriate power semiconductors.

This paper presents a study, sizing, and development of a DC-DC power converter for high-power solar PV applications. In this study, a DC-DC boost interleaved power converter with two arms controlled by an incremental conductance Maximum Power Point Tracking (MPPT) control algorithm is proposed. The MPPT is combined with a Proportional-Integral (PI) controller for individual control of the current on each arm and was applied to extract the maximum power available at the solar PV module for different solar radiation and temperature conditions. The digital control system was implemented in a TMS320F28335 microcontroller from Texas Instruments.

Keywords: DC-DC boost interleaved converter, Incremental conductance MPPT, PI controller, Renewable Energies, Solar photovoltaic system.

1 Introduction

Renewable energy sources play a key role in the *Roadmap for Carbon Neutrality 2050* [1]. This roadmap establishes, in a sustained way, the path to achieving carbon neutrality in 2050, defining the main guidelines and identifying the cost-effective options to achieve the intended result in different socio-economic development scenarios. Achieving carbon neutrality implies, together with other measures, the total decarbonization of the electro-producing system. At the end of 2021, Portugal closed its last coal-based power plant in operation, the Pego thermoelectric plant [2]. It is also committed to achieving a target of 80 % of the energy produced from renewable energy. However, according to ADENE, this target can be brought forward to 2025 [3].

Solar photovoltaic (PV) modules produce electricity from solar energy. They are composed of a combination of PV cells associated in series and/or parallel to obtain higher power units, as presented in [4]. Analyzing the electrical model of a solar PV cell, it is possible to verify that it has a current source operating mode. Therefore, It the integration of a power electronics converter, with constant input current, that guarantees a continuous extraction of the energy of the solar PV module, allows greater efficiency of the system [5].

This work presents a study on multi-string solar PV systems configurations, DC-DC boost interleaved converter, Incremental Conductance (IC), and proportional-integral (PI) algorithms with experimental validation. This project aims to contribute to the design and implementation of a power converter solution capable of integrating a high-power solar PV system. This document is organized into five sections, as follows: Section 1 introduces the subject; Section 2 describes the implemented power converter; Section 3 presents the simulations on the number of arms, switching frequency, and control circuit; Section 4 shows the experimental validations and in Section 5, the main conclusions are presented.

2 Proposed Converter

2.1 Solar PV System Configurations and Hardware Components

Solar PV systems can be configured in a variety of ways, namely centralized, string and ac-module configurations [6]. For high-power applications multi-string configuration stands out. The multi-string structure described in Fig. 1 has several strings of solar PV modules connected in series, interfaced with their DC-DC power converter to a common dc-ac power converter. This configuration uses only one dc-ac power converter, a lower cost, and greater simplicity and flexibility when compared to other configurations while allowing the application of the Maximum Power Point Tracking (MPPT) control algorithm individually.

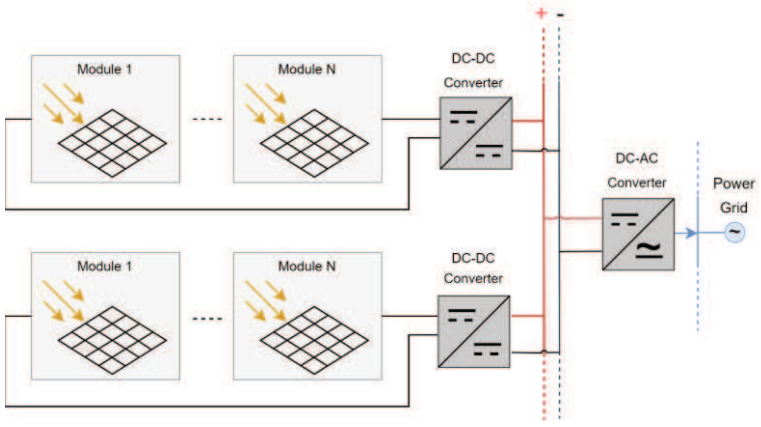

Fig. 1. Solar PV system based on multi-string configuration (based on [6]).

A very important aspect in the design of a power converter is related to the hardware to be used, namely the power semiconductors. Newer technologies such as silicon carbide (SiC) and gallium nitridet (GaN) offer advantages compared to other technologies such as insulated-gate bipolar transistor (IGBT), especially for high-power applications, highlighting smaller losses, better conductivity, and operation at higher temperatures, which results in more compact power converters [7]. Since both technologies serve the purpose of the application and SiC is presently more accessible than GaN, this technology is proposed in the current work [8].

2.2 DC-DC Interleaved Boost Converter

In all studied topologies such as conventional boost [9], cascaded boost [10], switched-capacitor boost [11], switched-inductor boost [12], the DC-DC interleaved boost converter (IBC) topology presents several advantages for high-power applications. In this topology, the output of the power converters is associated in parallel, which allows for achieving higher power values than when used separately.

Among the advantages of this topology, the smallest ripple of the input current and the output voltage stand out [13]. The current in each arm also has a lower value, which implies lower ohmic losses in the inductances, with greater efficiency and lower cost (due to a lower use of copper). When the current ripple is small, the input power becomes practically constant allowing for continuous energy extraction from solar PV modules.

In equation (1), the operation duty cycle (D) is represented as a function of the ratio of the input voltage (V_i) to the output voltage (V_o). On the other hand, Fig. 2 compares the ripple values of the current to different arm numbers (N) and semiconductor operation D. Thus, is possible to conclude that the use of a two-arm IBC allows for halving the maximum ripple of the input current when compared to the use of only one arm [13].

$$D = 1 - \frac{V_i}{V_o} \tag{1}$$

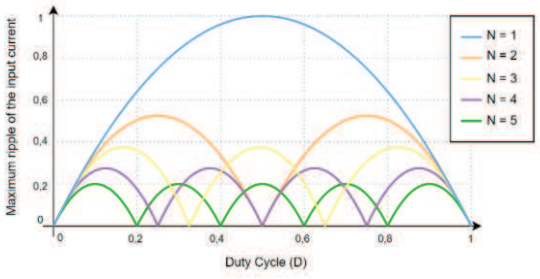

Fig. 2. Ripple of input current depending on duty cycle (D) and the number of arms (N) that composes the power converter.

To explain the principle of operation of the DC-DC IBC, a two-arms DC-DC IBC was used, as shown in Fig. 3. It consists of two conventional boost power converters

connected in parallel to operate alternately. The inductor L_1, the metal-oxide-semiconductor filed-effect transistor (MOSFET) S_1, and the diode D_1 form the first converter, while the inductor L_2, the MOSFET S_2, and the diode D_2 form the second converter. Each MOSFET device presents an internal free-wheeling diode. The two-arm DC-DC IBC shares the same capacitor, C_1, at the output. The phase-shift angle of the MOSFET pulse width modulation (PWM) signal is given by 360º/N, being N the number of arms of the power converter. In the case of two-arm DC-DC IBC, the PWM signals of the MOSFET S_1 lags the PWM signal of MOSFET S_2 by 180º. In turn, the number of MOSFET in simultaneous conduction depends on the value of D.

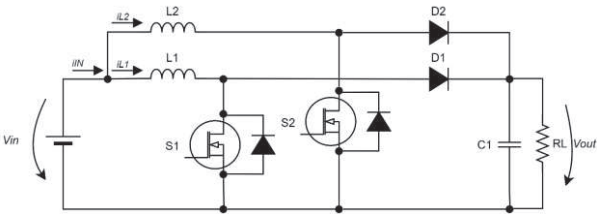

Fig. 3. Electrical schematic of the DC-DC IBC with two arms.

Fig. 4 presents the operation principle of the power converter for two operation modes: (i) Fig. 4 (a) for $D < 0.5$; (ii) and Fig. 4 (b) for D values ≥ 0.5. Considering the first condition, MOSFET never conducts at the same time. To study the behavior of the converter in this region, and consider the continuous conduction mode, it is possible to divide the operation into four stages [14]. Assuming that the parameters of the two converters are identical, a merely illustrative example of the theoretical waveforms of MOSFET control and currents in the inductors is shown in Fig. 4.

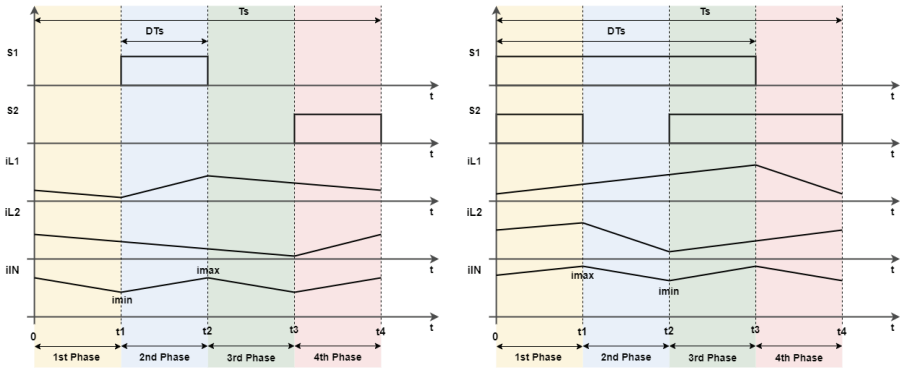

(a) (b)

Fig. 4. Theoretical waveforms of the DC-DC interleaved boost converter type with: (a) $D < 0.5$; (b) $D \geq 0.5$.

For this topology to operate within the expected specifications, it is necessary to correctly size the components. If the inductors have similar characteristics and the operation of the converter in CCM, their value can be calculated according to equation (2), where V_{in} is the converter input voltage, D is the duty cycle, N is the number of arms of

the converter, f_s is the switching frequency and $\Delta I_{L1,\,L2}$ is the current ripple on the respective inductor. Based on equation (3) it is possible to determine the value of the capacitor, being necessary to consider the value of the output current, *Iout*, which can be obtained using equation (4) [14].

$$L_1 = L_2 = \frac{V_{in}\,D}{N\,f_s\;\Delta I_{L1,L2}} \tag{2}$$

$$C\; = \frac{I_{Out}\,D}{N\,f_s\;\Delta V_{Out}} \tag{3}$$

$$\frac{I_{out}}{I_{in}} = 1 - D \tag{4}$$

2.3 MPPT Algorithm Based on Incremental Conductance Method

Among the various algorithms, there are two that stand out among the others: Perturbation and Observation (P&O) and Incremental Conductance (IC) [15]. Based on the bibliographic study, it is possible to conclude that both methods present a simple algorithm with good performance regardless of the operating conditions. However, the IC method has an additional advantage in the fact that voltage remains constant as soon as the maximum power point (MPP) is reached and reacts to greater temperature and radiation variations [16]. Authors present in [17] a c-code of the IC MPPT control algorithm integrated into a microinverter.

3 Simulation Results

This section presents the simulations of the proposed converter. Table 1 shows the general specifications of the DC-DC IBC. From these specifications, and the study of the interleaved boost converter made in section 2.2, it is possible to scale the number of arms of the converter as well as its main components' values. In addition, these specifications allow selecting one of the possible modules to use and the number of modules per string. 1500 V PV system has been identified as the most advantageous solution for high power installations [18][19][20]. Therefore, the proposed topology is in line with these new technological trends.

Table 1. General parameters of the simulations.

Parameter	Value	Unit
Nominal Input Voltage (V_{Nin})	1200	V
Open Circuit Input Voltage (V_{OCin})	1500	V
Input Current (I_{in})	12	A
DC Bus Output Voltage (V_{out})	2000	V
Input Current Ripple (ΔI_{in})	10	%
Output Voltage Ripple (ΔV_{in})	1	%

Replacing the DC-DC IBC input and output voltage values in equation (4), a *D* of 40 % is obtained. Components such as inductors and MOSFET devices can only be

selected after determining the number of arms of the DC-DC IBC since the current that crosses them is directly related to this parameter.

3.1 Study on the Number of Arms

As stated in section 2.2, the number of arms influences the input current ripple. Simulations were then performed, with a switching frequency (f_s) of 40 kHz, for different numbers of arms. Table 2 shows the values of the inductors and capacitors calculated based on equations (2) and (3), respectively, for the different numbers of arms and specifications of Table 1. Analyzing the data, it is possible to conclude that for the same operating conditions the greater the number of arms, the lower the value of the passive components. The simulation results for one, two, three, and five arms are present in Fig. 5.

Table 2. Capacitor and inductor values to a different number of arms.

Number of Arms	L (mH)	C (µF)
1	10	3.6
2	5	1.8
3	3.3	0.9
5	2	0.72

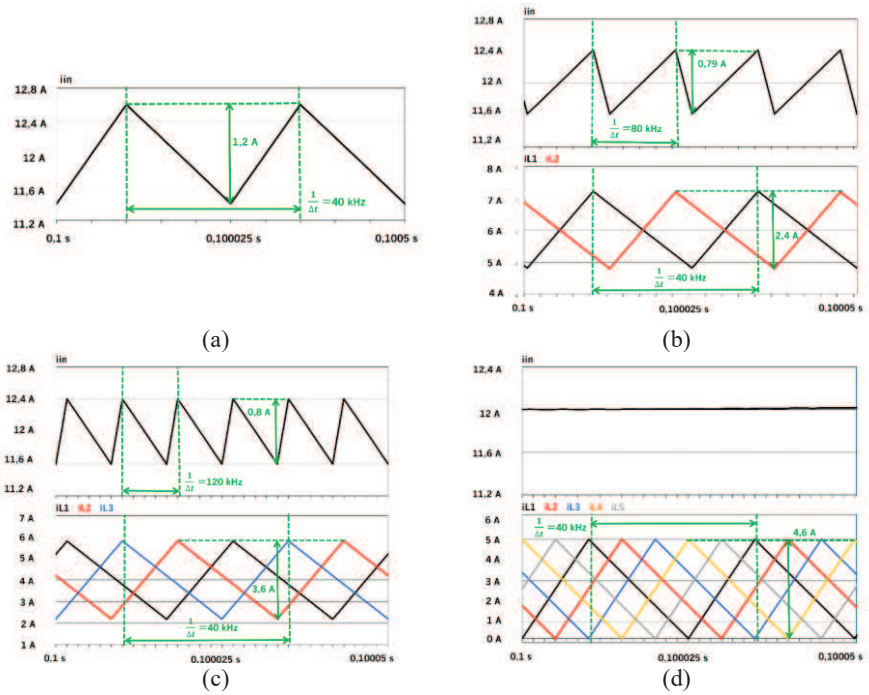

Fig. 5. Simulation results for different arm numbers, *fs* = 40 kHz: (a) 1 arm; (b) 2 arms; (c) 3 arms; (d) 5 arms.

As can be seen in Fig. 5 for a $D = 0.4$ case, the five-arm interleaved converter is the one with the smallest input current ripple, ($I\Delta_{in}$). Topologies with two and three arms have very similar and better results than the one-arm converter. It is important to note that a larger number of arms implies a higher failure probability as well as a higher implementation cost. However, a larger number of arms allows for greater redundancy. That is, in the event of a one-arm failure, if the converter does not have any additional arms, the system may operate in excess load or even fail to function. Given all these factors, one chose to develop a two-arm IBC. The two-arm converter solution allows for validation of the concept of interleaved without major implementation costs.

3.2 Study on the Switching Frequency

From Table 1 is known that the power converter has a maximum input current of 12 A and an output voltage of 2000 V. Once established the use a two-arm IBC power converter it is possible to select the value of the inductors and power semiconductors, SiC in this particular case. The main criterion for selecting the value of the inductor and the frequency to be used is the value of the losses in the inductors and SiC. In a DC-DC IBC with a 10 % ripple, the inductor losses (P_L) do not vary significantly with frequency. The main cause for losses is the winding internal dc resistance, R_{DC}. It is possible to calculate the inductor power losses using equation (5), where I is the root mean square value of the current that crosses the inductor, in this case as the current is almost constant there is no difference between rms and dc values. Switching and conduction losses in SiC MOSFET can be estimated using the PSIM tool which allows the selected semiconductor model to be inserted [21].

$$P_L = R_{DC}\ I^2 \text{ (W)} \tag{5}$$

Each inductor must be able to support the maximum current in each arm, which is half of the input current, i.e., 6 A. Thus, a set of 10 A high-frequency "197 DC series" inductors from Hammond Manufacturing [22] was selected, where the main characteristics are presented in Table 3. Nevertheless, the table also shows the frequency and output capacitor values calculated based on equations (2) and (3), respectively, for the different values of the inductors.

Table 3. Hammond Manufacturing series 10 A dc inductors.

L (mH)	DC Resistance (mΩ)	P_L (W)	Frequency (kHz)	C (µF)
1	232	8.352	200	1.8
3.5	293	10.548	57.1	1.03
7.5	403	14.508	26.7	0.72

Similarly, each SiC MOSFET will also have to conduct a current of 6 A and withstand a voltage equal to the dc-link voltage, 2000 V. It was thus decided to use the G2R120MT33J SiC from GeneSic [23], capable of supporting 3300 V and conducting 33 A.

Table 5 contains the values obtained in the simulation of conduction and switching SiC losses, inductor losses, and total losses, corresponding to the sum of the last three. Since the current ripple obtained for the three cases is virtually equal, the criterion for selecting f_s and the inductor to be used is related to the total losses of the circuit. Analyzing the results can be concluded that the lower losses occur for the inductor with 7.5 mH and a switching frequency of 26.7 kHz.

Table 4. Calculation of the total power losses concerning the inductance and switching frequency.

L (mH)	Frequency (kHz)	P_L (W)	$P_{switching}$ (W)	$P_{conduction}$ (W)	Total Losses (W)
1	200	8.352	226.9	1.97	237.2
3.5	57.1	10.548	60.05	1.71	72.31
7.5	26.7	14.508	28.46	1.75	42.72

3.3 Control Circuit

In a two-arm IBC, the real value of each arm inductor may be slightly different. Since the current must divide into each arm in a balanced way, two proportional-integral (PI) controllers are used to regulate the current in each arm as balanced as possible.

3.4 PSIM Solar PV Physical Model

As referred to in section 1 and the system specifications presented in Table 1, namely short-circuit input current and nominal input voltage, a monocrystalline silicon solar PV module, the LG Neon 2 of 350 W [24] was selected. This solar PV module has a 35.3 V voltage at the maximum power point (V_{mpp}) for the standard test conditions. Therefore, was implemented a simulation model using a solar PV physical model on PSIM, considering the main specifications of the LG Neon 2. Once the parameters of a solar PV module were completed, a string with 34 modules in series was configured, thus constituting the high voltage solar PV panel with a total voltage on the MPP of 1200 V and a maximum power of 11900 W.

3.5 Complete Circuit

Fig. 6 presents the diagram of the complete circuit. The MPPT algorithm block puts in the output a reference current that subtracted from the current of each arm will produce the error signals, *Error1* and *Error2*. Each error signal is applied to a PI and its output is compared with a triangular modulating waveform, producing a PWM signal that will command the SiC MOSFET. As explained in chapter 2.2, the modulating waveforms are 180° shifted.

The circuit was simulated for solar radiation intensity variations over time, as presented in Fig. 7. It is possible to observe, that the power at the output of the module, p_{in}, accompanies the maximum power, p_{max}, for the operating conditions. The same is true for the current at the output of the module, i_{in}, which tends to follow the calculated

reference current, i_{ref}. The maximum ripple current is within the expected specifications.

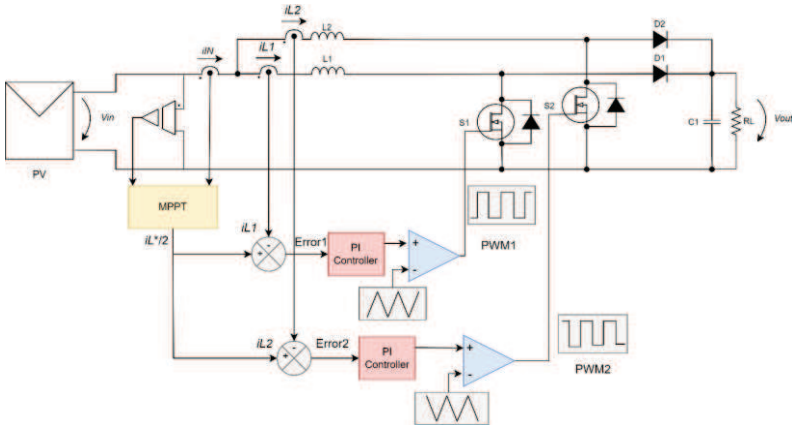

Fig. 6. Schematic diagram of the complete circuit.

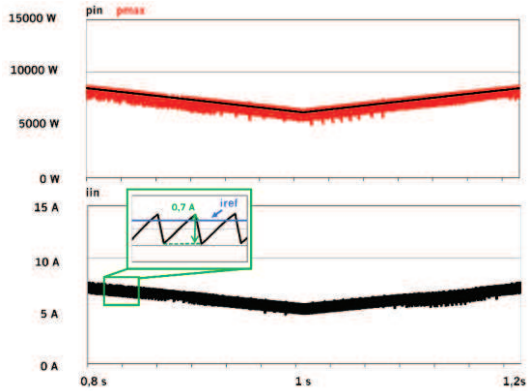

Fig. 7. Simulation of the circuit for variant operating conditions over time with detail of the input current ripple. Module output power, $p_{in;}$ maximum power for operating conditions, p_{max}; output module current, $i_{in;}$ reference current, $i_{ref.}$

In this section, the experimental results obtained from the system are exposed and analyzed. Results are analyzed in a fragmented way, namely the blocks necessary for the operation of the system, such as converter, PI and MPPT algorithms, and integration with the PV solar module.

4 Experimental Validation

This section describes the development and experimental validation processes of the two-arm IBC prototype. Prototype specifications, presented in Table 5, have been adapted to 1:30 scale reduction compared to the general specifications presented in Table 1.

Adopting a maximum input ripple current (ΔIin) of 10 %, based on equation (2), the minimum value for the switching frequency is 3.3 kHz. This is a relatively low value, so was chosen a frequency of 20 kHz, resulting in a ripple of 1.7 %. The printed circuit board (PCB) developed using Altium software is shown in Fig. 8.

Table 5. Prototype specifications.

Rated input voltage (V_{N_in})	40 V
Open circuit input voltage (V_{OC_in})	50 V
Input current (I_{in})	5 A
Output voltage on the DC bus (V_{out})	66 V
Inductor (L)	6 mH
Capacitor (C)	20 µF

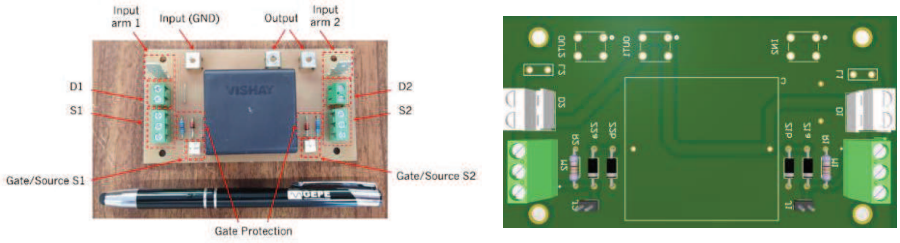

(a) (b)

Fig. 8. PCB developed for the DC-DC converter of the interleaved boost type: (a) PCB; (b) Altium 3D model.

The interface circuit between the gate driver output and the power semiconductor gate, as well as the gate protection circuit is composed by a gate-source 10 kΩ resistor, and a 16 V zener diode. The zener diode will protect the SiC in case there are gate voltages higher than allowed by the semiconductor. In turn, the resistor must avoid unwanted transitions in the event of PWM signal failure, imposing the SiC always on cut. It is important to note that the gate resistor is already on the driver circuit side, with a value of 12 Ω, so it has not been placed on the developed PCB.

Fig. 9 illustrates the control and power systems integration. The developed PCB and all the components present were attached to a wooden base to facilitate its fixation, organization, and transport. It should be mentioned that each signal conditioning box has four inputs for sensors: two current sensors and two voltage sensors. For this reason, a second signal conditioning box was used to be able to measure i_{in}.

4.1 Power Converter Tests

Preliminary tests to validate the developed hardware were carried out, proving the correct functioning of the open loop system. After, it was validated, initially with a PI control algorithm, to prove its correct operation, imposing a similar current on each arm and them the system was validated with the MPPT control algorithm activated, initially

in a controlled laboratory environment and, later, connected to a solar PV module. The results obtained are analyzed in the following topics.

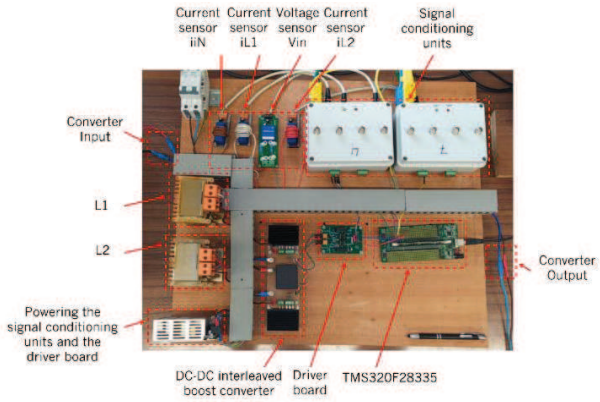

Fig. 9. Integrated system of DC-DC interleaved boost converter.

4.1.1 PI Algorithm Tests

To validate the PI algorithm and establish the proportional and integral gains, the test was divided into two stages. In the first one, a 2.25 A reference current was established. Analyzing Fig. 10 (a), it is possible to conclude that I_{in} presents an average value of 2.2 A, obtaining an average value of 1.07 A on i_{L1} and 1.08 A on i_{L2}. Concerning Fig. 10 (b), it is possible to observe the ripple current in each arm for these operating conditions. The correct functioning of the system can be concluded by obtaining a current close to the reference as well as a similar current in each arm.

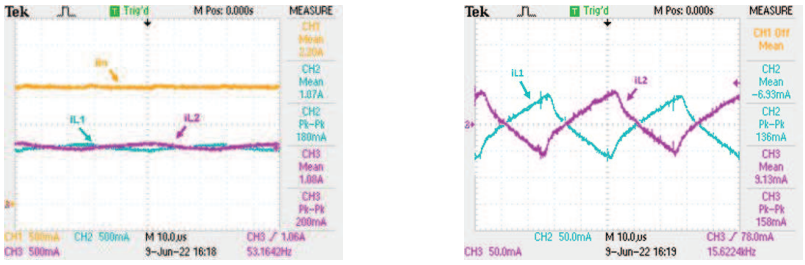

(a) (b)

Fig. 10. Experimental results of the PI algorithm with a reference current of 2.25 A: (a) Average value of the currents in each arm, i_{L1} and i_{L2}, and at the input, i_{in}; (b) Ripple of the current on each arm, i_{L1} and i_{L2}.

In the second stage, the reference was varied between 1.5 A and 3.75 A in an interval of 5 seconds with the same operating conditions. Analysing Fig. 11 (a) it is possible to see that the system follows the reference current. Regarding Fig. 11 (b) and Fig. 11 (c), it can be concluded that the establishment time is approximately 50 ms.

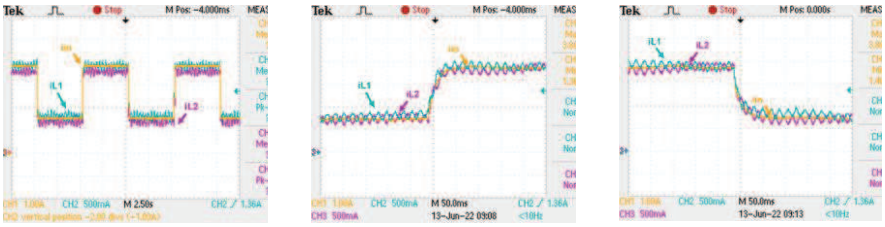

(a) (b) (c)

Fig. 11. Experimental results of the PI algorithm with a reference current varying between 1.5 A and 3.75 A: (a) Currents on each arm, i_{L1} and i_{L2}, and at input, i_{in}; (b) Currents on each arm, i_{L1} and i_{L2}, and at the input, i_{in}, in response to the upward current step; (c) Currents on each arm, i_{L1} and i_{L2}, and at the input, i_{in}, in response to the upward rung of current.

4.1.2 MPPT Tests

After validating the PI controller and adjusting the PI gains, MPPT tests were performed. For this purpose, a circuit with a rheostat (R_{in}) in series with the voltage source was implemented, as shown in Fig. 12. Therefore, when the rheostat voltage (v_r) is equal to the input voltage (v_{in}), the maximum power is extracted [25].

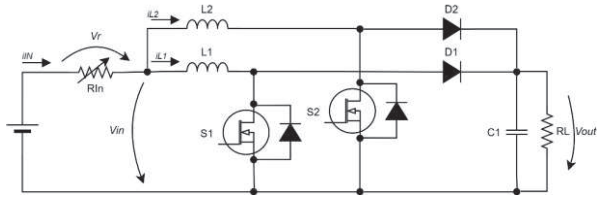

Fig. 12. Scheme used to test MPPT.

The test conditions were 30 V at the voltage source and 28 Ω at the output load, R_L. The test was divided into two parts. The first part consisted of keeping R_{in} equal to 11 Ω and evaluating whether v_{in} and v_r tended to 15 V. In Fig. 13 (a), it is possible to observe that shortly after starting the operation v_{in} and v_r converge to the same value. In Fig. **13** (b), it is possible to observe the currents i_{IN}, i_{L1} and i_{L2} in steady state, whereas in Fig. 13 (c) it turns out again that v_{in} and v_r have the value of 15 V.

In the second part, the objective was to record the response of the MPPT and the controller to sudden oscillations of the input parameters. Therefore, the R_{in} was varied between 8 Ω and 12 Ω. It can be seen in Fig. 14 that at the time instant demarcated with a red line that I_{in} decreased, but v_{in} and v_r remain approximately at the same value, demonstrating a correct functioning of the MPPT algorithm.

4.1.3 PV Solar Module Tests

The experimental validation was carried out by connecting the power converter to a solar PV module from BP Solar available in the laboratory [26]. From the BP 2150S

module, it is important to highlight a maximum power of 150 W, a 34 V voltage at a maximum power of, and a 4.45 A current at MPP. To make a comparison between the results obtained and the point of the actual MPP of the solar PV module, a test was performed in which the duty cycle of the controlled semiconductors was varied and the current and voltage at the converter input was recorded. Analyzing Fig. 15 (a) and (b) it can be concluded that the maximum power point is close to 28 V and 2.85 A. Fig. 16 shows the results obtained with the BP 2150S module at 1:26 pm. Analyzing the figure and keeping in mind the maximum power point previously withdrawn (28 V, 2.85 A) it is possible to conclude that the MPPT was successful since the values are very similar.

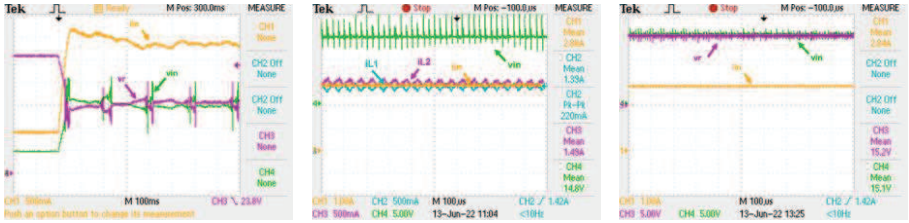

(a) (b) (c)

Fig. 13. Experimental results of the MPPT with R_{in} =11 Ω: (a) Voltage in resistance (v_r), Input voltage (v_{in}) and Input current (i_{in}) at the instant the MPPT is connected; (b) Input voltage (v_{in}), currents on each arm and at permanent entry; (c) Voltage in resistance (v_r), Input voltage (v_{in}) and Input current (i_{in}) in the permanent regime.

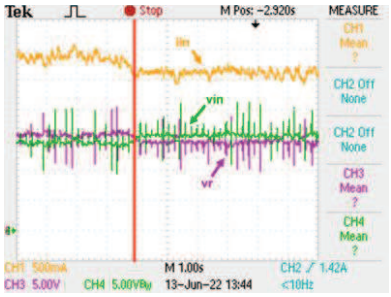

Fig. 14. Experimental results of MPPT when *varying* $R_{in:}$ Voltage in resistance (v_r), Input voltage (v_{in}) and Input current (i_{in}).

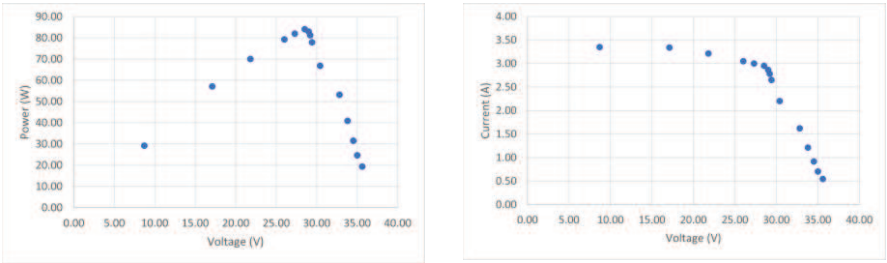

(a) (b)

Fig. 15. Results obtained when varying the duty cycle: (a) P-U Curve; (b) Curve I-V.

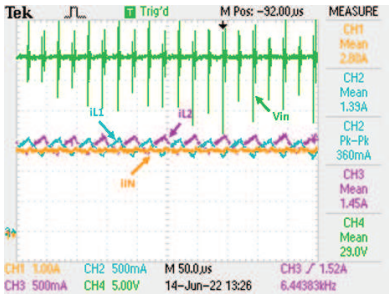

Fig. 16. Results obtained with the BP 2150S module at the 1:26 pm.

5 Conclusions

This paper aims to contribute to the analysis, design and development of a DC-DC power converter for high power solar photovoltaic (PV) applications. A two-arm interleaved topology was chosen, presenting the entire procedure performed for the design of the system. Regarding the control algorithms, the incremental conductance for the Maximum Power Point Tracking (MPPT) control algorithm was used in order to always extract the maximum power from the solar PV system. In turn, in order to impose a balanced current on each arm of the DC-DC power converter, a proportional-integral (PI) control algorithm was implemented. Simulation and experimental results prove the correct functioning of the system. It is concluded that this paper will contribute as a step-by-step guide for engineering students and engineers who intend to develop power electronics solutions for solar PV systems.

Acknowledgements

This work has been supported by FCT – Fundação para a Ciência e Tecnologia within the R&D Units Project Scope: UIDB/00319/2020. This work has been supported by the MEGASOLAR Project POCI-01-0247-FEDER-047220. Mr. Luis A. M. Barros is supported by the doctoral scholarship PD/BD/143006/2018 granted by the Portuguese FCT foundation.

References

[1] "Roteiro para a Neutralidade Carbónica 2050." [Online]. Available: https://www.portugal.gov.pt/pt/gc21/comunicacao/documento?i=roteiro-para-a-neutralidade-carbonica-2050-. [Accessed: 04-Mar-2022]

[2] "″Acabou″: Central do Pego produziu energia a carvão pela última vez." [Online]. Available: https://www.jn.pt/local/noticias/santarem/abrantes/acabou-central-do-pego-produziu-energia-a-carvao-pela-ultima-vez-14338710.html. [Accessed: 23–09-2022]

[3] J. V. Rodrigues, “Portugal pode ter 80% da energia de fontes renováveis já em 2025.” [Online]. Available: https://www.dinheirovivo.pt/empresas/portugal-pode-ter-80-da-energia-de-fontes-renovaveis-ja-em-2025-14604140.html. [Accessed: 04-Mar-2022]

[4] W. De Soto, S. A. Klein, and W. A. Beckman, “Improvement and validation of a model for photovoltaic array performance,” *Solar energy*, vol. 80, no. 1, pp. 78–88, 2006.

[5] L. A. M. de Barros, “Desenvolvimento de um microinversor com armazenamento local de energia para aplicações solares fotovoltaicas,” Universidade do Minho, 2016.

[6] F. J. da Costa Padilha, “Topologias de Conversores CC-CC Não Isolados com Saidas Simétricas para Sistemas Fotovoltáicos,” *Programa de Pós-graduaçã em Engenharia Elétrica, COPPE, Universidade Federal do Rio de Janeiro*, 2011.

[7] T. J. Sousa, V. Monteiro, B. Nova, F. Passos, J. Cunha, and J. L. Afonso, “Parallel Association of Power Semiconductors: An Experimental Evaluation with IGBTs and MOSFETs,” in *2019 International Young Engineers Forum (YEF-ECE)*, 2019, pp. 8–13.

[8] M. Beheshti, *Wide-bandgap semiconductors: Performance and benefits of GaN versus SiC*, ADJ 4Q. Texas Instruments, 2020.

[9] M. Forouzesh, Y. P. Siwakoti, S. A. Gorji, F. Blaabjerg, and B. Lehman, “Step-up DC-DC converters: a comprehensive review of voltage-boosting techniques, topologies, and applications,” *IEEE transactions on power electronics*, vol. 32, no. 12, pp. 9143–9178, 2017.

[10] M. Bhunia, R. Gupta, and B. Subudhi, “Cascaded DC-DC converter for a reliable standalone PV fed DC load,” in *2014 IEEE 6th India International Conference on Power Electronics (IICPE)*, 2014, pp. 1–6.

[11] Y. Hu and A. Ioinovici, “Simple switched-capacitor-boost converter with large DC gain and low voltage stress on switches,” in *2015 IEEE International Symposium on Circuits and Systems (ISCAS)*, 2015, pp. 2101–2104.

[12] O. Abdel-Rahim, M. Orabi, E. Abdelkarim, M. Ahmed, and M. Z. Youssef, “Switched inductor boost converter for PV applications,” in *2012 Twenty-Seventh Annual IEEE Applied Power Electronics Conference and Exposition (APEC)*, 2012, pp. 2100–2106.

[13] R. Buerger, A. Péres, R. Hausmann, R. Reiter, and A. Stankiewicz, “Ripple analyze and design considerations for an interleaved boost converter (IBC) for a PV source,” in *International Conference, ICREPQ*, 2014.

[14] Y. Jang and M. M. Jovanovic, “Interleaved Boost Converter With Intrinsic Voltage-Doubler Characteristic for Universal-Line PFC Front End,” *Power Electronics, IEEE Transactions on*, vol. 22, no. 4, pp. 1394–1401, 2007.

[15] N. K. M’Sirdi, A. Rabhi, and B. Nehme, “Review of the Best MPPT Algorithms for Control of PV Sources-RUCA Tracking Algorithm.,” in *ICINCO (1)*, 2017, pp. 318–325.

[16] D. Mustafi’c, D. Joki’c, S. Lale, and S. Lubura, “Implementation of Incremental Conductance MPPT Algorithm in Real Time in Matlab/Simulink Environment with Humusoft MF634 Board,” in *2020 9th Mediterranean Conference on Embedded Computing (MECO)*, 2020, pp. 1–5.

[17] L. A. Barros, M. Tanta, T. J. Sousa, J. L. Afonso, and J. Pinto, “New multifunctional isolated microinverter with integrated energy storage system for PV applications,” *Energies*, vol. 13, no. 15, p. 4016, 2020.

[18] E. Gkoutioudi, P. Bakas, and A. Marinopoulos, “Comparison of PV systems with maximum DC voltage 1000V and 1500V,” in *2013 IEEE 39th Photovoltaic Specialists Conference (PVSC)*, 2013, pp. 2873–2878.

[19] U.-M. Choi and T. Ryu, “Comparative evaluation of efficiency and reliability of single-phase five-level NPC inverters for photovoltaic systems,” *IEEE Access*, vol. 9, pp. 120638–120651, 2021.

[20] J. He, A. Sangwongwanich, Y. Yang, and F. Iannuzzo, “Enhanced reliability of 1500-v photovoltaic inverters with junction temperature limit control,” in *2021 IEEE 12th Energy Conversion Congress \& Exposition-Asia (ECCE-Asia)*, 2021, pp. 243–249.
[21] PowerSim, *Tutorial: Loss Calculation and Transient Analysis of SiC and GaN Devices*. PSIM, 2018.
[22] H. Mfg., “High frequency reactors (197 series).” [Online]. Available: https://www.hammfg.com/electronics/transformers/choke/197
[23] GeneSiC, “Datasheet: G2R120MT33J 3300 V 120 ohm SiC MOSFET,” 2021.
[24] LG, “Datasheet: LG Neon 2 350W I 345W,” 2019.
[25] S. Singer, S. Efrati, M. Alon, and D. Shmilovitz, “Maximum Electrical Power Extraction from Sources by Load Matching,” *Energies*, vol. 14, no. 23, p. 8025, 2021.
[26] bp solar, “Datasheet: BP 2150S,” 2001.